Journal of Materials Chemistry C

PAPER

View Article Online
View Journal | View Issue

Cite this: J. Mater. Chem. C, 2015, 3, 9393

Laser irradiation-induced modification of the amorphous phase in GeTe films: the role of intermediate Ge–Te bonding in the crystallization mechanism†

Seung Jong Park,[a] Hanjin Park,[b] Moon Hyung Jang,[c] Min Ahn,[a] Won Jun Yang,[a] Jeong Hwa Han,[a] Hong-Sik Jeong,[d] Cheol-Woon Kim,[b] Young-Kyun Kwon*[b] and Mann-Ho Cho*[a]

Received 17th April 2015,
Accepted 10th August 2015

DOI: 10.1039/c5tc01081k

www.rsc.org/MaterialsC

Modified amorphous GeTe, formed by the pulsed laser irradiation of as-grown GeTe, was analyzed in terms of variations in the local bonding structure using Raman spectroscopy and X-ray absorption fine structure in tandem with first-principles density functional theory. Amorphized GeTe (acquired from the crystalline phase) was compared with the modified amorphous GeTe to investigate the similarities and discrepancies between these two amorphous phases. Raman spectroscopy showed that these materials have a similar distribution of Ge-centered local structure in both phases, which is mainly composed of an octahedral-like structure. However, extended X-ray absorption fine structure results show the presence of a unique second type of Ge–Te bonding in the amorphized GeTe, which can effectively reduce the energy required for recrystallization. A computational study based on molecular dynamics simulations verified our experimental observations, including the existence of a second type of Ge–Te bonding in the amorphized phase. Moreover we distinguished the structural characteristics underlying the different amorphous phases, such as local atomic configurations and structural symmetries.

1. Introduction

Phase changes that occur in chalcogenide materials, including S-, Se- and Te-based alloys, have been extensively investigated because these phenomena induce changes in the electrical resistivity and optical reflectivity of the materials.[1,2] In particular, pseudo binary GeTe–Sb_2Te_3 alloys along a tie-line have phase change characteristics that show reversible phase transitions between the amorphous and crystalline phases on a time scale of a few nanoseconds.[3] To date, pseudo binary alloys, particularly $Ge_2Sb_2Te_5$, have been utilized in the production of non-volatile memory devices and optical disks.[4] Alloys such as $GeSb_2Te_4$, $Ge_2Sb_2Te_5$ and $GeSb_4Te_7$ along the same tie-line show similar crystallographic characteristics indicating metastable and stable crystal structures that are characterized by their cubic and hexagonal lattices, respectively.[5,6]

The local structure of Ge atoms in GeTe–Sb_2Te_3 materials is important in terms of explaining the phase change between amorphous and crystalline structures, *i.e.*, the reversible change in the local structure of the Ge atom between tetrahedral and octahedral local structures in the amorphous and crystalline phases, respectively. Likewise, other elements (Sb and Te) can also be described by their local structures, in which the octet rule and the non-octet rule are obeyed in the amorphous and crystalline phases, respectively. However, in several studies, difficulties arose related to the local structure of the amorphous phase in defining the crystallization mechanism, including symmetry changes, due to deviations between the amorphous phase of the as-grown film and the amorphized phase from the crystalline structure. Previous studies on the amorphization of the crystalline structure induced by pulsed laser irradiation show that the local structure of Ge atoms is similar to that of the crystalline phase; this similarity leads to a lower activation energy and a more rapid crystallization.[7–9] Therefore, a reversible phase transition can no longer be described by the transition between tetrahedral and octahedral local structures. The amorphized phase introduces a defective octahedral local structure for Ge atoms, in which the bonding symmetry is similar to that for the octahedral structure, but has a lower coordination number than that of the crystalline phase.[10] In this sense, if it was possible

[a] Institute of Physics and Applied Physics, Yonsei University, Seoul 120-749, Republic of Korea. E-mail: mh.cho@yonsei.ac.kr
[b] Department of Physics and Research Institute for Basic Sciences, Kyung Hee University, Seoul, 130-701, Republic of Korea. E-mail: ykkwon@khu.ac.kr
[c] Department of Material Science and Engineering, University of Pennsylvania, Philadelphia 19104, USA
[d] School of Integrated Technology, Yonsei University, Incheon 406-849, Republic of Korea

† Electronic supplementary information (ESI) available. See DOI: 10.1039/c5tc01081k

to modify the Ge-centered local structure of the as-grown amorphous phase, the modification could allow the crystallization characteristics to deviate from those of the as-grown amorphous phase. There have been several attempts to permanently modify the amorphous phase using energetic ion and photo irradiation. The results of these studies indicate the presence of local minima in the amorphous structures that have a sufficient energy barrier above the thermal energy. De Bastiani *et al.* carried out modifications of the GeTe amorphous structure using Ge^+ ion irradiation and showed that the modified amorphous GeTe is largely composed of an octahedral-like Ge local structure with a reduction in tetrahedral Ge atoms.[11] In addition, the kinetics of crystallization of the ion irradiated GeTe were different from as-grown amorphous GeTe and behave similar to the partially crystallized samples. Similarly, the amorphization process for the GeTe-based chalcogenide materials induced an abnormal crystallization, the mechanism of which deviated from the as-grown amorphous phase.[12,13] Although the modifications of the Ge local structure lead to a different crystallization mechanism, the remaining question is whether the presence of a defective local structure such as an octahedral-like structure can only describe the different recrystallization mechanism of the amorphized phase. The recrystallization mechanism of the amorphized phase in the case of GeTe-based materials may be more complex, because it has been reported that the amorphization process from a crystalline phase can generate medium range ordering.[9] Therefore, a comparative study on the structural nature between the modified and amorphized phases would offer insights into the instability of the amorphized phase and the recrystallization mechanism. Pulsed laser irradiation is an effective method that can modify the local structure of the as-grown amorphous phase without causing any long-range ordering. In this study, modified amorphous GeTe obtained from an amorphous structured sample was compared with amorphized GeTe obtained from a crystalline structure. This comparison allows us to determine any similarities and/or discrepancies between the local structural characteristics of these two phases. In the recrystallization mechanism, we confirmed that the presence of an intermediate Ge–Te bonding in the amorphized structure makes an important contribution and leads to a reduction in the crystallization temperature.

2. Experimental

A GeTe film (80 nm thick) was deposited on a thermally grown SiO_2 300 nm/Si(100) substrate at room temperature by ion beam sputtering deposition (IBSD) using a single GeTe target. The atomic concentrations and contaminating elements were determined by Rutherford backscattering spectrometry (RBS) and *in situ* photoemission spectroscopy (XPS). These showed well-matched target compositions without any contaminating elements. Without breaking the vacuum, a SiO_2 capping layer (25 nm thick) was sequentially deposited *via* IBSD to minimize any oxidation that might occur in the annealing process and the atmospheric measurement conditions. For acquiring a crystalline phase, annealing was conducted in an N_2 atmosphere using a rapid thermal process (RTP), where the isothermal duration was retained for 15 minutes at 250 °C. These conditions exceeded the crystallization temperature, as confirmed by X-ray diffraction. To induce structural modification in the as-grown amorphous film and amorphization of crystalline phases, a KrF pulsed laser (wavelength = 248 nm, duration = 25 ns) was irradiated in a direction normal to the sample surface. The irradiation process was conducted under a pressure of 1×10^{-7} Torr *via* a sapphire window. The energy of the pulsed laser was set to values (energy densities) that are able to trigger a phase transition in the polymorphic phases. To minimize energy variations, the irradiated area was maintained, with a beam aperture, in the form of a 10 mm × 10 mm square. Raman spectroscopy was employed utilizing backscattering geometry to verify microstructural changes in the crystal structure, with a visible Raman spectroscopy system (LabRam Aramis, Horriba Jovin-Yvon) with an ND:Yag laser (wavelength = 532 nm). The power of the probing laser was limited to below 2 mW to eliminate thermal effects in the probing region. The change in resistance as a function of annealing temperature was measured with a constant heating rate of 6 K min^{-1} using a two-point contact method, and the temperature was recorded using a thermocouple in contact with the sample surface. In order to investigate changes in the local bonding structure around the Ge atoms that had undergone the modification, crystallization and amorphization processes, X-ray absorption near-edge structure (XANES) and extended X-ray absorption fine structure (EXAFS) experiments were performed at the 8C beamline of the Pohang Accelerator Laboratory (PAL) in Korea. The Ge reference foil was measured every moment to calibrate the E_0 of the Ge K-edge before the loading of the GeTe sample. Ge K-edge X-ray absorption spectra were acquired in the range of 0–15 K using the fluorescence mode with a seven-channel Ge detector.

3. Computational methods

To identify several amorphous phases of GeTe and their local atomic structures, we performed molecular dynamics (MD) simulations under various conditions, including different temperatures, densities, and diverse initial configurations. The MD simulations were carried out within a canonical ensemble using *ab initio* density functional theory (DFT)[14] based on a linear combination of atomic orbitals, as implemented in the SIESTA code.[15,16] We solved the classical equation of motion with the quantum mechanical force acting on each atom, calculated by the Hellmann–Feynman theorem. The target temperature was controlled by adjusting the temperature of the heat bath using a Nosé thermostat.[17–20] A double-ζ polarization was used as a basis set to expand the electronic wave functions. The behavior of valence electrons was described by a norm-conserving Troullier–Martins pseudopotential[21] in the Kleinman–Bylander factorized form.[22] $4s^24p^2$ and $5s^25p^4$ electrons for Ge and Te are considered as a valence level in pseudopotential. We used the Perdew–Zunger form[23] of the Ceperley–Alder exchange–correlation (XC) functional[24] in the local density approximation (LDA).

The charge density and potentials were determined on a real-space grid with a mesh cutoff energy of 210 Ry. We used a confinement energy shift of 0.01 eV, which defines the cutoff radii of the atomic orbitals.

With several structures having a relatively low potential energy among those thermally equilibrated amorphous phases obtained by the MD simulations, we carried out geometry relaxation to find the corresponding equilibrium structures using DFT, as implemented in the Vienna ab initio simulation package (VASP).[25,26] The projector augmented wave potential[27,28] was employed to describe the valence electrons, and the electronic wave functions were expanded by a plane wave basis set with a cutoff energy of 400 eV. The XC functional was treated with LDA as used for SIESTA. To find the equilibrium configurations, all of the geometries were optimized without any symmetry constraints using the conjugate gradient method[29] until none of the residual Hellmann–Feynman forces acting on any atom exceeded 0.01 eV $Å^{-1}$. In our calculations, we chose a supercell containing 128 atoms as a unit cell, which forms a distorted rock-salt or rhombohedral lattice with lattice angles of $\alpha = \beta = \gamma = 58.36^{\circ}$. The lattice constant was adjusted phase by phase. To estimate energy barriers between any two phases, we applied the variable cell nudged elastic band (NEB) method[30,31] with the initial and final structures obtained by geometry relaxation.

4. Results and discussion

4.1 Experimental analysis of the local structure in various amorphous phases

Fig. 1(a) shows the non-polarized Raman spectra with six fitting curves for the as-grown and its modified GeTe films produced by laser irradiation. The Raman mode of the as-grown film indicates the existence of specific Raman active modes at around 80, 110, 160 and 220 cm^{-1}, corresponding to the amorphous phase of the GeTe film.[11] Structural modifications induced by external perturbations, such as thermal energy and electromagnetic waves, effectively lead to a shift in and a distortion of the Raman spectrum. The laser irradiation slightly modified the Raman modes around 110 and 160 cm^{-1}, indicating structural deviations from the initial structure of the amorphous phase (but not crystallization). In the case of amorphous GeTe, the Raman modes were primarily characterized by the tetrahedral bonding structure of Ge and two-fold Te chains. In the fitting process, six Gaussian curves, denoted as I, II, III, IV, V and VI, were used to describe the spectrum between 60 and 300 cm^{-1}, which is in agreement with previous Raman studies.[11,32] Since the phonon lifetime of the disordered material is a random distribution, as opposed to a finite value, the line shape of the Raman mode can be described by a Gaussian contribution. The fitting parameters of the as-grown and modified (irradiated) GeTe films are summarized in Table S1 (ESI†). The fitted result clearly shows that laser irradiation resulted in changes in the relative intensity and the full width at half maximum (FWHM). Moreover, unknown additional curves (patterned curve) and a slight shift ($\lesssim$3 cm^{-1}) were also observed. The additional curves minimize the chi-square

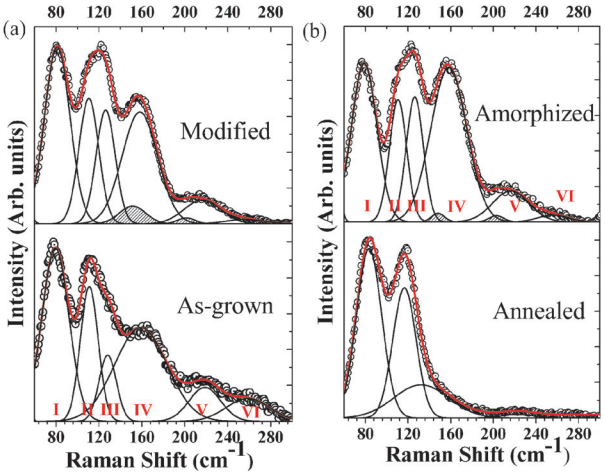

Fig. 1 (a) Variation in the non-polarized Raman spectra of as-grown and modified amorphous GeTe films. Fitting results based on 6 Gaussian contributions, denoted as I–VI. (b) Raman spectra of annealed and irradiated (amorphized) GeTe films, showing that laser irradiation leads to the collapse of the E_g and A_{1g} modes of the rhombohedral structure in the annealed film, indicating amorphization.

of the fitting process, which could indicate an arising asymmetry of curves IV and V, but not the formation of new features. In fact, irradiation and/or ion implantation can effectively induce anharmonicity in bond distribution as well as bonding geometry.[33] Andrikopoulos *et al.* suggested that the Raman active modes of the amorphous GeTe originate from the stretching and bending modes of the tetrahedral local structure of Ge atoms, indicating a T_d point group.[32] The sp^3 valence electrons of the tetrahedral Ge atoms are saturated in the form of $GeTe_{4-n}Ge_n$, with a statistical distribution that is based on the random bonding model. However, the assumption of valence electron saturation with a bonding geometry of $GeTe_{4-n}Ge_n$ is insufficient for describing the real amorphous structure of the GeTe film. In a previous extended X-ray absorption fine structure (EXAFS) study of as-grown amorphous films, the coordination number of Ge atoms in GeTe was found to be less than 4, while that of $Ge_2Sb_2Te_5$ was closer to 4. In this sense, Kolobov *et al.* suggested the coexistence of octahedral-like 3(Ge):3(Te) and tetrahedral 4(Ge):2(Te) in as-grown amorphous GeTe films, based on EXAFS results.[34] In a recent study, the Raman spectrum of the amorphous GeTe was calculated by *ab initio* simulations and empirical bond polarizability.[35] Although the model of the amorphous structure was formed by a melt-quenching process within *ab initio* MD, the calculated phonon density of the state accurately describes the Raman spectrum of as-grown amorphous GeTe. The *ab initio* calculation indicates that the main Raman modes below 190 cm^{-1} (given by two modes around 120 and 165 cm^{-1}) are mainly due to the vibration of defective octahedra, while the lower intensity above 190 cm^{-1} is caused by tetrahedral local structures. Therefore, fitting curves II, III and IV are directly related to the octahedral-like geometry (and not the tetrahedral geometry) of the sample. The additional curve I at 80 cm^{-1} is mainly generated by the vibrational mode associated with three-fold Te atoms. Alternatively, fitting curves V and VI, above

190 cm^{-1}, can be assigned to a tetrahedral geometry.[35] However, in the case of the tetrahedral $GeTe_3Ge_1$ unit, the vibrational (bending) modes can also be partially attributed to the IV band. As a result, a one-to-one exchange of contributions between the III and VI Raman modes suggests that irradiation induces a modification in the bonding symmetry in the Ge-centered local structure from tetrahedral to octahedral-like structures. Moreover, the distributions of Ge–Ge homopolar bonds in tetrahedral $GeTe_{4-n}Ge_n$ affect the frequency of the tetrahedral stretching mode. That is, a higher frequency mode is indicative of a larger number of homopolar bonds in the tetrahedral structure. In particular, the changes in the Raman mode show that tetrahedral $GeTe_{4-n}Ge_n$ with a higher Ge portion can easily soften and be transformed into an octahedral-like symmetry by irradiation. Although the symmetry changes do not indicate deviations from the sp^3 valence structure, changes in the Ge local structure containing modified bond angles are more similar to the directionality of a p-bond system than the bonding structure of an amorphous phase. The crystal structure of GeTe can be represented by a rhombohedral lattice (space group *R3mH*, No. 160), which is defined by its alpha-phase as a metastable structure. As a result, the enhancement in the octahedral-like symmetry for the Ge-centered geometry suggests that the modified amorphous phase shows an increased similarity with the crystalline phase, compared with the as-grown phase. Likewise, several studies associated with amorphous structures have shown that the local structure of the amorphous phase, acquired from the crystalline phase *via* melt-quenching and laser irradiation, maintains the same local crystalline geometry and shows a strong similarity in its point symmetry (*e.g.*, octahedral-like and/or pyramidal symmetry).[8,10,36] In addition, the changes of the local structures lead to variations in the crystallization temperature (or a reduction of the activation barrier for crystallization) and speed.[9,37] Therefore, similarities and discrepancies between the local structures can provide information related to the phase change mechanism.

The amorphous phase can initially be transformed into a rhombohedral structure as a metastable phase that can also be represented by a distorted rocksalt structure. The Raman modes of the annealed GeTe film show three Gaussian contributions that are composed of two main bands (82.5 and 116.5 cm^{-1}) and the additional broad band (133.1 cm^{-1}), as shown in Fig. 1(b). The curve fitting for the crystalline phase was conducted under the same fitting frame with the same Gaussian distributions as were used for the as-grown and modified amorphous phases. The high frequency modes such as IV, V and VI in the amorphous phase completely disappear, indicating an absence of tetrahedral $GeTe_{4-n}Ge_n$ in the annealed film. That is, the tetrahedral structure is transformed into an octahedral structure that effectively forms a crystalline phase with a rhombohedral lattice (refer to X-ray diffraction results as shown in Fig. S2, ESI†). In addition, the Raman modes of the annealed film failed to be fitted by the III and IV modes any more, unlike amorphous phases, which indicates a reduction in the defective octahedral local structure with a coordination number lower than 4. Group theory obviously predicts the E_g and A_{1g} modes ($\Gamma = A_1 + E$) of the rhombohedral structure, which accurately indicates two main bands in the annealed film. Moreover, the long-range Te–Te interaction with the atomic distance of 4.23 Å in the crystalline phase generates additional vibrational modes at 133.1 cm^{-1}, which can be described by the phonon density of states in the Te chain model.[38] The effect of irradiation on the crystalline phase clearly leads to the collapse of long-range ordering, which can be defined as amorphization phenomena. This is dissimilar from the slight modification of the as-grown amorphous phase without phase transformation. The broad curve at 132 cm^{-1} in the crystalline phase originates from vibrations of the Te chain.[38] The collapse of the rhombohedral structure, driven by irradiation, generates Raman active modes (denoted as V and VI) due to the tetrahedral $GeTe_{4-n}Ge_n$. An additional curve is also observed with a lower intensity than that of the modified amorphous phase. Furthermore, it should be noted that the modes of octahedral-like symmetry (denoted as I, II and III) appear to be directly connected with the E_g and A_{1g} modes of the rhombohedral crystalline phase. In the rhombohedral structure, the A_{1g} (non-degenerated) and E_g (doubly degenerated) modes correspond to a modulating displacement along the C_3 axis and the axis perpendicular to the C_3 axis, respectively. In particular, the A_{1g} mode represents the Peierls distortion mode, which can also be assigned to the rhombohedral A7 structure of group V (As, Sb, and Bi).[39,40] Peierls distortion leads to periodic bond pairing from 6-fold to 3-fold bonding, inducing rhombohedral distortion of the cubic structure and generating van der Waals forces along the C_3 axis in rhombohedral structures. The release of the Peierls distortion is accompanied by volumetric changes in the rhombohedral lattice, which reduces the frequencies of two phonon modes (phonon softening).[41] In this context, variations in the coordination number under mediated Peierls distortion affect the frequency. Upon the collapse of long-range ordering, the splitting of the Peierls distortion mode (around 120 cm^{-1}) can be related to the coordination number associated with octahedral-like symmetry, despite the fact that the Peierls distortion can be defined in space with periodicity. Similar to the modified amorphous phase, the contribution of curve VI to the amorphized phase is considerably weaker. The existence of curve VI is prominent in the as-grown phase, which suggests that the tetrahedral unit, with a high Ge content, does not participate in the reversible phase transition between the amorphous and crystalline phases. In this respect, the amorphized phase is quite similar to that of the Ge-centered bonding geometry, which is composed of an octahedral-like symmetry in the modified amorphous phase. However, curve IV indicates relatively high contributions compared to those of the modified amorphous phase. Since the contribution and the linewidth of curve IV cannot be linearly correlated with curves II and III, additional vibrational (bending) motions should be introduced into the 160 cm^{-1} mode to describe the increasing intensity of curve IV with decreasing width. In a previous study on amorphization induced by distortion, it was reported to be possible for the rotations of cubic fragments to lead to an amorphization process.[42] After the initial stage, Ge–Ge bonding is formed in the diagonal direction in the form of a $GeTe_3Ge$ unit, and the structural unit gradually relaxes into tetrahedral symmetry. In the presence of long-range

ordering, the Ge–Te cubic fragments are rapidly transformed from a p-bonded structure to an sp^3 hybridized structure due to energetic stability. Therefore, once the long-range ordering has collapsed, despite the fact that amorphization is initiated by the distortion of broken resonant bonding, the tetrahedral $GeTe_3Ge$ structure forms naturally from the crystalline phase. The transition of Ge bonding symmetry between the octahedral and tetrahedral structures was also confirmed by XANES, as shown in Fig. S2 (ESI†). The Raman and XANES spectra showed a strong similarity between the modified and amorphized phases.

EXAFS analyses can provide more information on radial distribution from a selected central atom by considering single scattering paths with neighboring atoms. Fig. 2(a) shows the Fourier transformed (FT) magnitude of the EXAFS signal for the Ge K-edge in the as-grown and modified amorphous GeTe films. The main bonding environment of the Ge atoms is composed of Ge–Ge and Ge–Te bonding structures, which agrees well with previous reports.[34,43] The average coordination number is less than 4, indicating the presence of a 3-fold geometry. However, the bond length along the radial direction (single scattering) of Ge–Te cannot provide any information about the bonding geometry. Moreover, the formation of the Ge–Ge bond in the amorphous phase confuses the classification between tetrahedral Ge–Te and pure tetrahedral Ge–Ge structures. X-ray photoemission spectroscopy (XPS) is typically used for investigating discrepancies between homopolar and homo-/heteropolar mixtures of bonding structures, because the pure-bonding and mixture-bonding structures in tetrahedral bonded materials (group IV alloys) are precisely separated from the purely tetrahedral bonding structures.[44] Alternatively, the bond length is maintained under distributions of the homo-/heteropolar bonding structures. *In situ* XPS analysis clearly shows that there is no pure Ge–Ge homopolar bonding structure (refer to Fig. S3, ESI†) and only Ge–Te bonding structures with different environments are present. Therefore, the Ge–Ge homopolar bonding based on EXAFS originates from the tetrahedral $GeTe_{4-n}Ge_n$ bonding structures. In addition, the definition of Ge–Ge bonds in the amorphous phase is informative because the Raman mode denoted as IV (260 cm^{-1}) in Fig. 1(a) has conventionally been assigned to amorphous-like Ge–Ge bonding,[32] which can be correlated with 4-fold Ge–Ge bonding (based on EXAFS results). In the case of modified amorphous GeTe, the bond length of the central Ge atoms remains without a large deviation after irradiation. This corresponds to a slight modification of the Raman modes without new features. The reduction in the FT magnitude is mainly correlated with variations in the coordination number and the mean-square relative displacement along each bonding pair. Moreover, we considered the possibility that irradiation could lead to variations in the interatomic distribution of Ge–Te bonding as well as the bonding symmetry of Ge atoms. This can be associated with the generation of additional curves in the Raman mode. The fitting parameters for the EXAFS data are listed in Table S2 (ESI†).

As shown in Fig. 2(b), irradiation effectively leads to amorphization, which is in agreement with the Raman results. The Ge–Te bonding of the annealed film is clearly separated (2.79 ± 0.30 Å and 3.13 ± 0.58 Å), indicating bond pairing caused by rhombohedral deformation (or Peierls-like distortions). The amorphization induced by irradiation results in the disappearance of the crystalline bonding features. Moreover, the bond lengths of each bond pairing are completely transformed from an extended bond length to a shortened bond length, such as Ge–Te (2.63 ± 0.04 Å) and Ge–Ge (2.47 ± 0.02 Å), respectively, which show the local structure of the amorphous phase. However, the C_3 cumulant exhibits a negative value (−0.0052 ± 0.0022 $Å^2$) that is different from the modified amorphous phase, implying a skewed Gaussian distribution for the Ge–Te bonds. In addition, it is interesting that another Ge–Te bond is found at 3.30 Å, while no other Ge–Ge bonds occur above 3.0 Å. The Ge–Te bonding around 3.30 Å appears to be lengthened more than the long bond (3.13 Å, as defined in the fitting result) of Ge–Te in the rhombohedral crystalline phase. Another type of Ge–Te bonding can be defined as the level of the local bond involving distances longer than the nearest neighbor bond. Since a second Ge–Te bond has not been observed in the as-grown or modified amorphous phases, this constitutes a unique intermediate bonding feature of the amorphized phase. Akola *et al.* reported on bonding characteristics, including bond distribution and local bonding structures between constituent elements in melt-quenched GST and GeTe, using MD simulations.[36,45] The calculated distance–distance correlation map of the Ge–Te bonding pair clearly shows that the main Ge–Te bonding occurs around 2.8 Å with intermediate Ge–Te bonding distributions with a relatively low probability (broadening between 3.2 and 4.0 Å).[45] Likewise, the melt-quenched amorphous model of $Ge_2Sb_2Te_5$ also showed the formation of a pyramidal structure that includes the presence of an intermediate type of Ge–Te bonding (in the range of 3.0–3.5 Å) in addition to the main Ge–Te bonding.[8] Moreover, the amorphized phases of both GST and

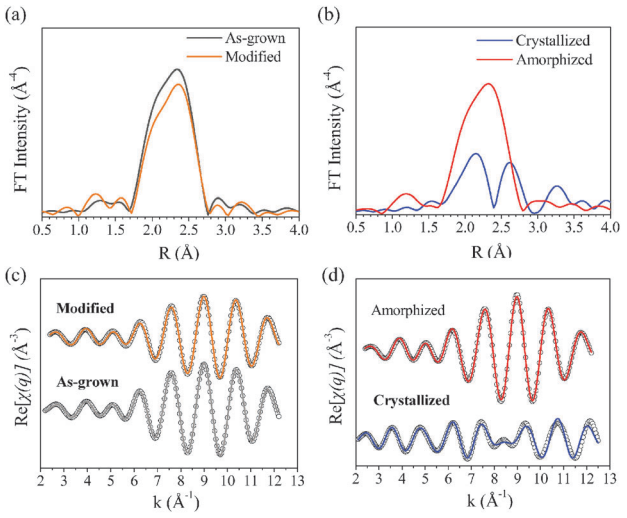

Fig. 2 Fourier-transformed magnitude of the Ge K-edge EXAFS for (a) as-grown and (b) annealed phases with irradiation effects. Fourier-filtered Ge K-edge EXAFS data (solid line) and fitting results (dotted line) for (c) as-grown and (d) annealed phases (including each irradiated phase).

GeTe have semi-order characteristics that can be based on the order parameter (0.5), but do not indicate periodicity.[45] Therefore, the intermediate Ge–Te bonding may act as a bridge (similar to intermolecular bonding) between local structural subunits. In other words, laser irradiation is able to transform the sp^3 hybridized bonding orbital into the non-hybridized p^3 bonding orbital in the amorphous phase containing intermediate Ge–Te bonding.

4.2 Computational analysis based on molecular dynamics simulation

To understand the local structure of each phase, we performed various MD simulations. The method for constructing the initial configuration of the as-grown and irradiated phases (amorphized and modified amorphous structures) is represented in the ESI.† We evaluated its radial distribution function (RDF) $g(r)$, which is an averaged distribution of the interatomic bond length, defined by

$$g(r) = \frac{1}{\rho}\left\langle \sum_{j\neq i} \delta(r - r_{ij}) \right\rangle \quad (1)$$

where ρ is the density and $\delta(x)$ a Dirac delta function. Here, means an ensemble average. Time average was also taken over ~3 ps, during which an MD simulation was performed after the structure was allowed to equilibrate at room temperature. Similarly, its partial RDF $g_{\alpha\beta}(\mathbf{r})$ analyzed between two elements α and β (α, β = Ge or Te) was calculated, as shown in Fig. 3. As seen in Fig. 3(a) and (b), there are little differences in the partial RDFs between the as-grown and modified amorphous phases, except for a few hundredths of an Å difference in their bond lengths, at which their partial RDFs have the maxima. It was, however, observed that there are conspicuous differences when compared to those of the crystalline (Fig. 3(c)) and amorphized (Fig. 3(d)) phases. Especially in the crystalline phase, only Ge–Te bonds were found for $r < \sim 3.6$ Å (and next Ge–Te bonds around $r \approx 5$ Å), while the Ge–Ge and Te–Te bonds peaked at around 4.23 Å, indicating the formation of the second-neighbor shell. Another interesting feature in the crystalline phase is that there are two types of Ge–Te bonds, one with a "short" bond of ~2.8 Å and another with a "long" bond of ~3.2 Å, as represented by two imaginary Gaussian curves in Fig. 3(c). In the three amorphous phases, on the other hand, a significant number of Ge–Ge bonds appeared with a bond length of around 2.5–2.7 Å. Moreover, only short Ge–Te bonds exist in the as-grown and the modified phases, whereas a contribution from long Ge–Te bonds was observed in the amorphized phase similar to the crystalline phase. This was verified by two Gaussian functions used for the fitting shown in Fig. 3(d). The long or second bonds were identified as bonding between the Ge central atom in the sub local unit and the Te bridge atom located in the middle of the structure shown in the inset of Fig. 3(d), while the short or first bonds were mainly observed within the sub local structures. The medium range order originating from Te–Te bonds observed in the crystalline phase still existed in the amorphous phases. The bond lengths estimated at their corresponding peaks in RDF are in good agreement with our EXAFS data.

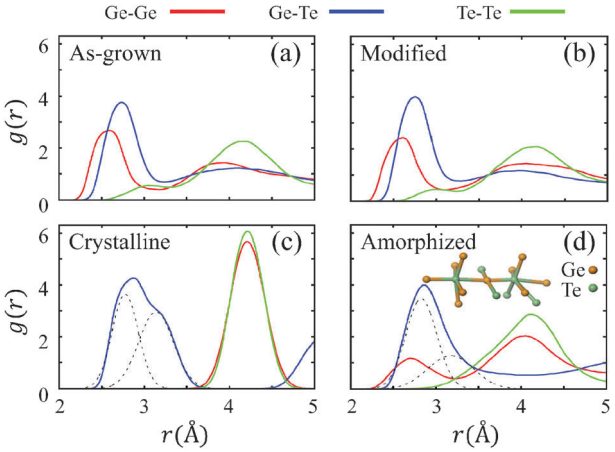

Fig. 3 Partial radial distribution functions (RDFs) analyzed between Ge–Ge, Ge–Te, and Te–Te at T = 300 K for (a) as-grown, (b) irradiated, (c) crystalline, and (d) amorphized phases. As indicated at the top, RDFs for Ge–Ge, Ge–Te, and Te–Te are represented by red, blue and green lines, respectively. The inset in (d) represents a typical local structure of the amorphized phase. There are two sub local units, in each of which a Ge atom is located at the center, connected to each other through a bridged Te atom in the middle. The long or second Ge–Te bonds correspond to the bonds between the center Ge atom in a sub unit and the bridge Te atom. The Ge and Te atoms are denoted by orange and green balls, respectively.

We evaluated the averaged partial coordination number (CN) $n_{\alpha\beta}$ of the α atom for the α–β bonds by integrating the partial RDF $g_{\alpha\beta}(\mathbf{r})$ as follows:

$$n_{\alpha\beta} = \rho_\alpha \int_0^\infty 4\pi r^2 \mathrm{d}r g_{\alpha\beta}(r) f(r) \quad (2)$$

where $f(r)$ is a "soft" cutoff function for the nearest neighbors defined by

$$f(r) = \frac{1}{1 + \exp[\kappa(r - r_c)]} \quad (3)$$

with r_c = 3.3 Å for the "hard" cutoff and the broadening parameter κ^{-1} = 0.05 Å. The calculated partial CNs are listed in Table 1. The CN of the α atom n_α was simply calculated by $n_\alpha = \sum_\beta n_{\alpha\beta}$. As the as-grown phase is being modified by irradiation, the Ge–Ge (Ge–Te) partial CN $n_{\mathrm{Ge–Ge}}$ ($n_{\mathrm{Ge–Te}}$) decreases (increases) from 1.69 (2.54) to 1.60 (2.73). Overall, n_{Ge} increases from 4.23 to 4.33, and n_{Te} from 2.99 to 3.11. This tendency was also observed in our experimental results. In the crystalline phase, neither Ge–Ge nor Te–Te homogeneous bonds are present, but only heterogeneous Ge–Te bonds. The amorphized phase exhibits quite different CNs from all the other phases. Its n_{Ge} and n_{Te} are 4.81 and 3.84.

To further identify the local topology of each phase, we computed the angular distribution (AD) for all types of trimers, β–α–γ (α, β, γ = Ge or Te) with the center atom α, as shown in Fig. S3 (ESI†). The AD values for the crystalline and the three amorphous phases were evaluated for all Ge- and Te-center atoms by taking an average over 3 ps in the MD simulations at T = 300 K. Ideal octahedral and tetrahedral structures have bond angles of 90° (and also 180°) and 109.4°, respectively, and

Table 1 Partial coordination numbers calculated for the four phases of GeTe

Phase	Ge–Ge	Ge–Te	Te–Ge	Te–Te
As-grown	1.69	2.54	2.54	0.45
Modified	1.60	2.73	2.73	0.38
Crystalline	0.00	5.22	5.22	0.00
Amorphized	1.08	3.73	3.66	0.18

such characteristic angles are marked with dotted lines in Fig. S3 (ESI†). In order to clarify the difference in AD among the different structures, they are shown as CN-resolved AD color maps, as shown in Fig. 4. The ADs of the as-grown, the modified, the amorphized, and the crystalline phases are displayed sequentially from the top to bottom row of the figure, while those of the total and all possible β–α–γ trimers are aligned column by column. For the as-grown and the modified phases, their local structures appear to be similar, as shown in Fig. 4(a–g) and (h–n). Ge center atoms mainly form four-coordinated bonds, while Te atoms prefer three-coordinated bonds. It is clear from the high population positions that both tetrahedral and octahedral structures are possible.

Combining AD populations with the CN values listed in Table 1, we further analyzed the local structures. After simple arithmetic calculations from the partial CNs in the respective phases, we estimated the contributions of various local bonding structures enclosing the center atom Ge or Te. For the as-grown and modified phases, the Ge center atom is mainly enclosed by $GeTe_3$, Ge_2Te_2, or Ge_2Te_3. Their corresponding portions are ~31% (~40%), ~46% (~27%), and ~23% (~33%), while ~45% (~38%), ~55% (~51%), and ~0% (~11%) of the Te center atoms combine with Ge_2Te, Ge_3, and Ge_4, respectively. From the local bonding structure estimations done on the two phases, it is possible to trace the role of laser irradiation in this process, which modifies the as-grown phase to a modified phase. Another interesting feature observed is that there is a two-fold Te-centered distribution with Ge–Te–Ge and Ge–Te–Te indicating the presence of Te chain structures in as-grown and modified phases.

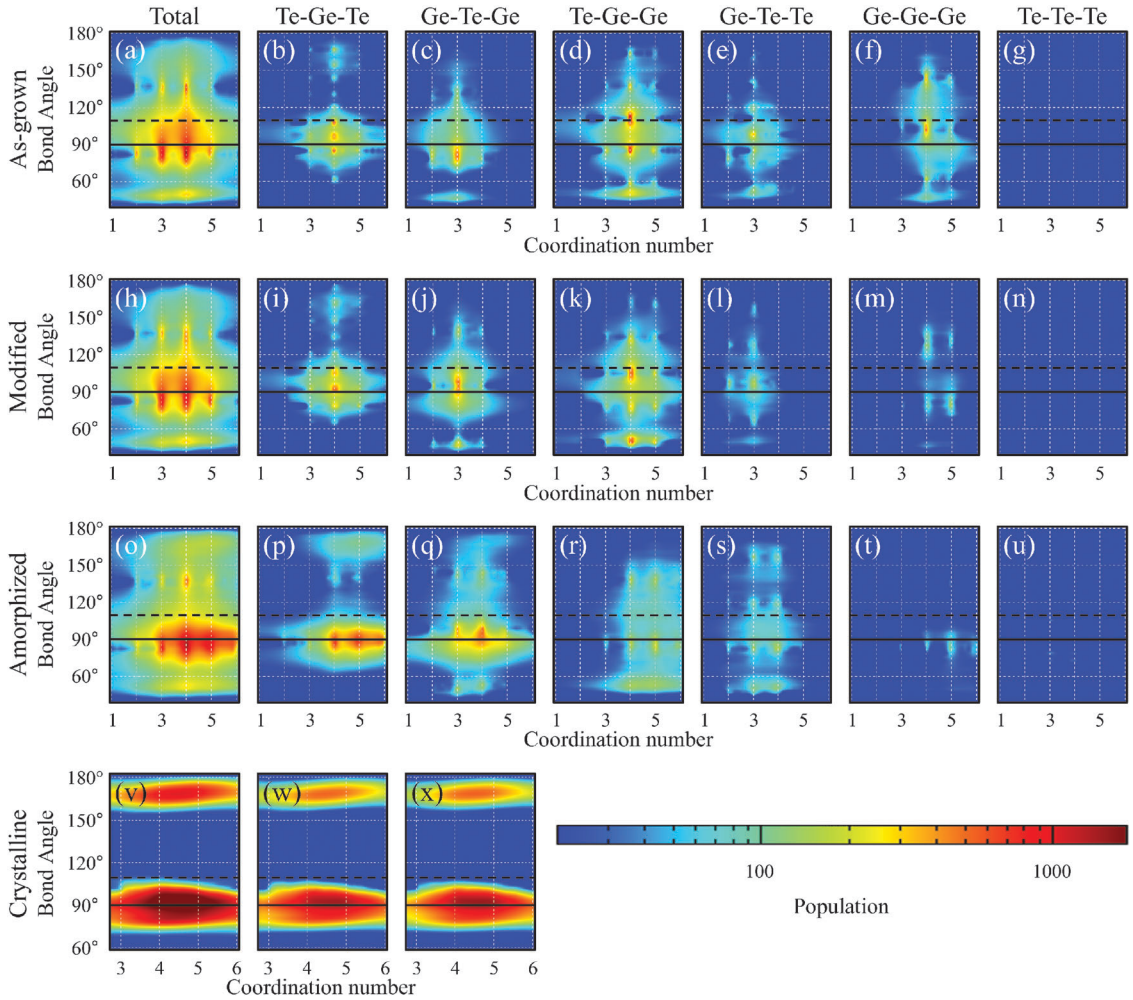

Fig. 4 Color-mapped population densities of angular distributions (ADs) resolved into the coordination numbers (CNs) for the as-grown (a–g), the modified (h–n), the amorphized (o–u), and the crystalline (v–x) phases. As indicated at the top, the first column represents the total population densities, and the following columns represent the population densities of Te–Ge–Te, Ge–Te–Ge, Te–Ge–Ge, Ge–Te–Te, Ge–Ge–Ge, and Te–Te–Te, respectively. The octahedral (tetrahedral) local ordering is indicated by a black solid (dashed) line. The color-mapped values are in a log scale.

The amorphized phase clearly shows noticeable differences in AD population plots shown in Fig. 4(o)–(u). We observed strong population peaks along the solid line at 90° in both the Te–Ge–Te and the Te–Ge–Te AD population color maps displayed in Fig. 4(p) and (q). As mentioned above, the amorphized phase has two types of Ge–Te bonds as shown in Fig. 3(d), and n_{Ge} = 4.81 from Table 1. All of these facts imply that both Ge and Te center atoms form mainly incomplete and deformed octahedral structures, rather than tetrahedral ones. Such a bonding characteristic originating from the crystalline phase is a unique feature of the amorphized phase, which distinguishes itself from the other two amorphous phases. As was similarly done for the as-grown and modified phases, we estimated its local bonding structures. ~27%, ~65%, and ~8% of central Ge atoms are enclosed by $GeTe_3$, $GeTe_4$, and Ge_2Te_4, respectively, while either Ge_3, Ge_3Te, or Ge_4 encloses the central Te atom with its corresponding portion of ~16%, ~18%, or ~66%, respectively.

In Fig. 4(v)–(x), the crystalline phase trivially displays its high population density values along the solid line at 90° and, to a lesser extent, below 180° indicating an octahedral order regardless of Ge or Te, since the GeTe crystalline structure forms a distorted rock-salt or rhombohedral lattice. Because there are no Ge–Ge and Te–Te bonds, but only symmetric Ge–Te bonds in the crystalline structure, the Ge-centered population density is essentially the same as the Te-centered structure.

4.3 Considering energy in crystallization from various amorphous phases

Our experimental and computational studies indicate that the modification of the as-grown amorphous phase effectively induces changes in the local bonding structure. That is, the local structure of Ge–Te(Ge) dominantly has an octahedral-like structure with the Ge–Ge bond portion being reduced by irradiation. On the other hand, the amorphized phase has not only a higher symmetry within the nearest neighbors, but intermediate Ge–Te bonds with a smooth distribution above 3.2 Å as well. As a result, the EXAFS and MD calculations showed a possible discrepancy with respect to the second type of Ge–Te bonding between both phases. It would be interesting to understand the nature of the structural origin of the activation energy. Although the crystallization temperature (with a single ramping rate) is directly connected to the activation energy, comparing the modified and amorphized phases is invaluable in terms of investigating the thermal stability necessary for maintaining an amorphous phase. In this context, it is possible to determine the correlations between the activation energy and the two structural features that are present in the octahedral-like structure and the role of intermediate bonding in the overall process.

Fig. 5(a) and (b) show the change in resistance as a function of increasing annealing temperature for a constant ramping rate of 8 K min^{-1}. As expected, the modified amorphous phase (induced by laser irradiation) shows a lower T_c value (20 K) than the as-grown amorphous phase. The pre-existence of a p^3 bonding structure, in combination with a reduction in sp^3 tetrahedral bonding, facilitates crystallization (*i.e.*, a lower

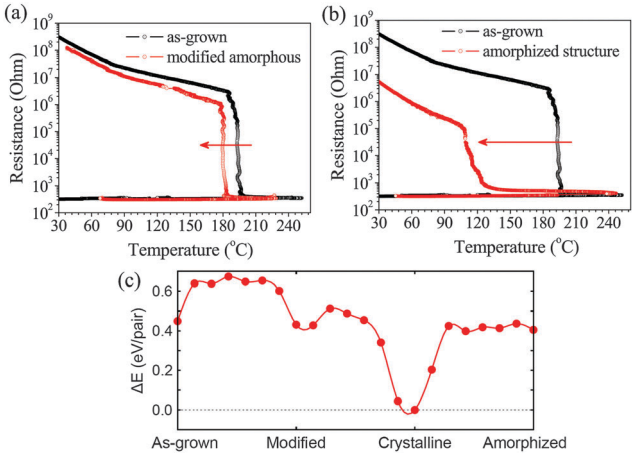

Fig. 5 Plot of sheet resistance as a function of annealing temperature for the (a) modified amorphous and (b) amorphized phases, relative to the as-grown amorphous phase. (c) Energy barrier for phase transition evaluated between the as-grown and modified, the modified and crystalline, and the crystalline and the amorphized phases using the nudged elastic band method.

thermal stability). This is caused by the similarity of the p-type bonding structures between the modified and crystalline phases. However, the T_c for the amorphized phase shifts down significantly by 80 K, as shown in Fig. 5(b). The significant shift in the T_c clearly indicates the effects of the similarities and discrepancies between the modified and amorphized phases. From the view point of the resistance drift, the reset state acquired from the melt-quenching process mostly experiences a gradual drift in resistance with time. Previous studies insisted that the resistance drift of an amorphous phase is related to the structural atomic rearrangement of the amorphous network that is correlated with an enhancement in disordering and bandgap widening. However, the detailed information concerning the structural rearrangement in the reset state is quite insufficient. Interestingly, the different types of amorphous phases, such as as-grown, modified and amorphized phases, can be ascribed to the structural characteristics of the Ge-centered local structure in this study, which also indicates that the electrical and optical properties of the amorphous phases can change by a small modification in the local structure. Therefore, the resistance drift in the reset state, which is accompanied by a structural rearrangement, is possibly correlated with the local structural changes. In this sense, we conclude that the presence of different types of amorphous phases provides the structural model of the resistance drift.

To study the phase transition between any of the two phases, we identified various local equilibrium configurations for three amorphous phases. During the MD simulations, we collected not only the atomic coordinates and velocity, but also the potential energy, which varies with the MD time steps. We chose several local minima of the potential energy, at which we carried out further geometry relaxation to identify the corresponding equilibrium configurations. Using these structures, we studied phase transition using the nudged elastic band (NEB)

method. The values for the energy barrier between two phases were evaluated to be ~0.25 eV, ~0.15 eV, ~0.5 eV, and ~0.1 eV, respectively, from the as-grown to the modified, from the modified to the crystalline, from the crystalline to the amorphized, and from the amorphized to the crystalline form. These energy barrier values are per Ge–Te pair. In order to obtain a firm estimate for the energy barrier corresponding to each phase transition, one should consider the realistic volume where phase change occurs. We also found that, interestingly, there are multiple activation barriers with similar energy barrier values in a single transition between any two phases, implying that a series of simultaneous steps were involved in the phase transitions. Although this barrier estimation does not correspond to the real activation barrier, the calculated per-pair values still distinguish the relative ease of the phase transitions.

Such relative energy barrier differences can be attributed to differences in the local structures. The presence of the second Ge–Te bonds in the amorphized phase decreases the activation barrier to the crystalline phase, in which the second type of Ge–Te bonds is also present. Following the umbrella flip model of the crystallization mechanism, Ge motion between tetrahedral and octahedral sites on an atomic scale would significantly facilitate crystallization.[46] This can also be understood as the transition between non-hybridized p^3 bonding and hybridized sp^3 bonding with respect to the formation of the bonding orbital. The crystal structure with a rhombohedral lattice (or distorted rocksalt) has a long Ge–Te bonding (3.13 Å in this study), which maintains the attraction of interlayers along the C_3 axis. The electron density vanishes midway along the Ge–Te bond, indicating the formation of van der Waals forces in the long Ge–Te bonding. The second intermediate Ge–Te bonding plays the role of a bridge between the local structural units and can reduce the energy required for interlayer attraction during crystallization.

5. Conclusions

Laser irradiation induces modifications in an as-grown amorphous phase. These changes are characterized by a transition between an octahedral-like local structure (or pyramidal structure) and a tetrahedral structure. Raman spectroscopy data indicate that the tetrahedral $GeTe_{4-n}Ge_n$ with a higher portion of Ge can easily soften and be transformed into an octahedral-like symmetry on irradiation. As a result, the modified amorphous phase, compared with the as-grown phase, shows an increased similarity with the crystalline phase. This similarity is also observed in the case of an amorphized phase that is produced from the crystalline phase by laser irradiation. Raman and XANES spectra clearly show that the modified and amorphized phases have similarities (*i.e.*, the presence of an octahedral-like structure with a high contribution). However, EXAFS results show a possible discrepancy with respect to medium range ordering between the modified and amorphized phases. That is, the amorphized phase has a second type of Ge–Te bonding with an anharmonic distribution around 3.30 Å, which plays a role in intermediate bonding. This second Ge–Te bonding acts as a bridge between the local structural units and can effectively reduce the energy required for attraction of the interlayer during crystallization.

The amorphized phase, including intermediate Ge–Te bonding, can be more easily disturbed than the as-grown amorphous phase, due to a reduction in the stability of the amorphous phase. These intermediate bonding sites function as seeds in the crystallization, but have a tradeoff relationship with the stability of the amorphous phase. In addition, the defective sites of the octahedral-like structure as well as the intermediate bonding state in the amorphized phase contribute to the formation of local minima, which explains why resistance drift can gradually occur in the reset states.

Acknowledgements

We gratefully acknowledge financial support from the Ministry of Trade, Industry & Energy (MOTIE) in Korea (Project No. 10045360) and Korea Semiconductor Research Consortium (KSRC) through the project of developing source technology for future semiconductor devices. Some portions of our computational work were done using the resources of the KISTI Supercomputing Center (KSC-2014-G2-001 and KSC-2014-C2-028).

References

1 S. Shaji, A. Arato, J. J. O'Brien, J. Liu, G. A. Castillo, M. I. M. Palma, T. K. Das Roy and B. Krishnan, *J. Phys. D: Appl. Phys.*, 2010, **43**, 075404.
2 M. M. Hafiz, O. El-Shazly and N. Kinawy, *Appl. Surf. Sci.*, 2001, **171**, 231.
3 N. Yamada, E. Ohno, K. Nishiuchi, N. Akahira and M. Takao, *J. Appl. Phys.*, 1991, **69**, 2849.
4 J. B. Park, G. S. Park, H. S. Baik, J. H. Lee, H. Jeong and K. Kim, *J. Electrochem. Soc.*, 2007, **154**, H139–H141.
5 O. G. Karpinsky, L. E. Shelimova, M. A. Kretova and J. P. Fleurial, *J. Alloys Compd.*, 1998, **268**, 112.
6 T. Matsunaga, R. Kojima, N. Yamada, K. Kifune, Y. Kubota, Y. Tabata and M. Takata, *Inorg. Chem.*, 2006, **45**, 2235.
7 V. Weidenhof, I. Friedrich, S. Ziegler and M. Wuttig, *J. Appl. Phys.*, 2001, **89**, 3168.
8 M. Krbal, A. V. Kolobov, P. Fons, J. Tominaga, S. R. Elliott, J. Hegedus and T. Uruga, *Phys. Rev. B: Condens. Matter Mater. Phys.*, 2011, **83**, 054203.
9 S. J. Park, M. H. Jang, S. J. Park, M. Ahn, D. B. Park, D. H. Ko and M. H. Cho, *J. Mater. Chem.*, 2012, **22**, 16527.
10 S. Caravati, M. Bernasconi, T. D. Kuhne, M. Krack and M. Parrinello, *Appl. Phys. Lett.*, 2007, **91**, 171906.
11 R. De Bastiani, E. Carria, S. Gibilisco, M. G. Grimaldi, A. R. Pennisi, A. Gotti, A. Pirovano, R. Bez and E. Rimini, *Phys. Rev. B: Condens. Matter Mater. Phys.*, 2009, **80**, 245205.
12 P. K. Khulbe, E. M. Wright and A. M. Mansuripur, *J. Appl. Phys.*, 2000, **88**, 3926.
13 H. Y. Cheng, S. Raoux and Y. C. Chen, *J. Appl. Phys.*, 2010, **107**, 074308.

14 W. Kohn and L. J. Sham, *Phys. Rev.*, 1965, **140**, A1133.
15 P. Ordejón, E. Artacho and J. Soler, *Phys. Rev. B: Condens. Matter Mater. Phys.*, 1996, **53**, R10441.
16 M. Soler, E. Artacho, J. D. Gale, A. Garc, J. Junquera, P. Ordej and S. Daniel, *J. Phys.: Condens. Matter*, 2002, **14**, 2745.
17 S. Nosé, *Mol. Phys.*, 1984, **52**, 255.
18 W. G. Hoover, *Phys. Rev. A*, 1965, **31**, 1695.
19 M. P. Allen and D. J. Tildesley, *Computer Simulation of Liquids*, Clarendon Press, New York, NY, 1989.
20 D. C. Rapaport, *The Art of Molecular Dynamics Simulation*, Cambridge University Press, Cambridge, 2nd edn, 2004.
21 N. Troullier and J. L. Martins, *Phys. Rev. B: Condens. Matter Mater. Phys.*, 1991, **43**, 1993.
22 L. Kleinman and D. M. Bylander, *Phys. Rev. Lett.*, 1982, **48**, 1425.
23 J. P. Perdew and A. Zunger, *Phys. Rev. B: Condens. Matter Mater. Phys.*, 1981, **23**, 5048.
24 B. J. Alder and D. M. Ceperley, *Phys. Rev. Lett.*, 1980, **45**, 567.
25 G. Kresse and J. Furthmüller, *Comput. Mater. Sci.*, 1996, **6**, 15.
26 G. Kresse and J. Furthmüller, *Phys. Rev. B: Condens. Matter Mater. Phys.*, 1996, **54**, 11169.
27 P. E. Blöchl, *Phys. Rev. B: Condens. Matter Mater. Phys.*, 1994, **50**, 17953.
28 G. Kresse and D. Joubert, *Phys. Rev. B: Condens. Matter Mater. Phys.*, 1999, **59**, 1758.
29 M. R. Hestenes and E. Stiefel, *J. Res. Natl. Bur. Stand.*, 1952, **49**, 409.
30 G.-R. Qian, X. Dong, X.-F. Zhou, Y. Tian, A. R. Oganov and H.-T. Wang, *Comput. Phys. Commun.*, 2013, **184**, 2111.
31 D. Sheppard, P. Xiao, W. Chemelewski, D. D. Johnson and G. Henkelman, *J. Chem. Phys.*, 2012, **136**, 74103.
32 K. S. Andrikopoulos, S. N. Yannopoulos, G. A. Voyiatzis, A. V. Kolobov, M. Ribes and J. Tominaga, *J. Phys.: Condens. Matter*, 2006, **18**, 965.
33 M. C. Ridgway, C. J. Glover, K. M. Yu, G. J. Foran, C. Clerc, J. L. Hansen and A. N. Larsen, *Phys. Rev. B: Condens. Matter Mater. Phys.*, 2000, **61**, 12586.
34 A. V. Kolobov, P. Fons, J. Tominaga, A. L. Ankudinov, S. N. Yannopoulos and K. S. Andrikopoulos, *J. Phys.: Condens. Matter*, 2004, **16**, S5103.
35 R. Mazzarello, S. Caravati, S. Angioletti-Uberti, M. Bernasconi and M. Parrinello, *Phys. Rev. Lett.*, 2010, **104**, 085503.
36 J. Akola and R. O. Jones, *Phys. Rev. Lett.*, 2008, **100**, 205502.
37 P. K. Khulbe, E. M. Wright and M. Mansuripur, *J. Appl. Phys.*, 2000, **88**, 3926–3933.
38 M. H. Brodsky, R. J. Gambino, J. J. E. Smith and Y. Yacoby, *Phys. Status Solidi B*, 1972, **52**, 5.
39 K. Ishioka, M. Kitajima and O. V. Misochko, *J. Appl. Phys.*, 2008, **103**, 123505.
40 A. A. Melnikov, O. V. Misochko and S. V. Chekalin, *Quantum Electron.*, 2013, **43**, 313.
41 X. Wang, K. Kunc, I. Loa, U. Schwarz and K. Syassen, *Phys. Rev. B: Condens. Matter Mater. Phys.*, 2006, **74**, 134305.
42 A. V. Kolobov, P. Fons and J. Tominaga, *Phys. Rev. B: Condens. Matter Mater. Phys.*, 2013, **87**, 165206.
43 Y. Maeda and M. Wakagi, *Jpn. J. Appl. Phys., Part 1*, 1991, **30**, 101.
44 A. Barranco, F. Yubero, J. P. Espinos, J. P. Holgado, A. Caballero, A. R. Gonzalez-Elipe and J. A. Mejias, *Vacuum*, 2002, **67**, 491.
45 J. Akola and R. O. Jones, *Phys. Rev. B: Condens. Matter Mater. Phys.*, 2007, **76**, 235201.
46 A. V. Kolobov, P. Fons, A. I. Frenkel, A. L. Ankudinov, J. Tominaga and T. Uruga, *Nat. Mater.*, 2004, **3**, 703.

